Science Advances

MAAAS

Supplementary Materials for

Transgene-free remote magnetothermal regulation of adrenal hormones

Dekel Rosenfeld, Alexander W. Senko, Junsang Moon, Isabel Yick, Georgios Varnavides, Danijela Gregureć, Florian Koehler, Po-Han Chiang, Michael G. Christiansen, Lisa Y. Maeng, Alik S. Widge*, Polina Anikeeva*

*Corresponding author. Email: anikeeva@mit.edu (P.A.); awidge@umn.edu (A.S.W.)

This PDF file includes:

Supplementary materials

SI-1: Finite Element Analysis

To determine the stimulation parameters i.e. stimulation duration, MNPs concentration and injection volume, needed to reach the TRPV1 threshold of 42 °C, we used finite element modeling (FEM). Pennes' bio-heat equation was used to account for the enriched blood perfusion within the adrenal gland tissue. The following equation was used in the model:

[1] $$\rho_A C_A \frac{\partial T}{\partial t} = K_A \nabla^2 T + \rho_b C_b w_b (T-T_b) + P$$

A-adrenal tissue, b-blood properties, f -ferrofluid, P - power density of heat source

Ferrofluid inside the adrenal gland tissue was modeled as a sphere with radius R. Ferrofluid is considered as a spherical heat source of constant power density P that is excited by the AMF. We calculated the temperature distribution in the tissue as function of the distance r and the temperature t. All the physical parameters used are in **Table S1**. P was calculated as:

[2] $$P = V_{ferrofluid} \cdot SLP \cdot_{ferrofluid} \cdot \rho_{ferrofluid}$$

where $V_{ferrofluidis}$ is the total volume of MNPs in the droplet, $\rho_{ferrofluid}$ is the density of ferrites (MNPs concentration) and SLP is the specific loss power for the MNPs in the examined AMF conditions of frequency $f = 515$ kHz and amplitude $H_0 = 15$ kA/m amplitude.

A layer of fat surrounds the adrenal tissue and rapidly grows in young adult rats over time. We therefore included a fat layer surrounding the adrenal tissue, which can influence the heat distribution with the gland. The adrenal gland was modeled as an ellipsoid with dimensions of $6 \times 2.4 \times 2.4$ mm^3 (with total volume of ~18 mm^3 based on previous studies (*41*)). An additional fat layer of 1.5 mm thickness was examined and the following equations were used:

[3] $$\rho_A C_A \frac{\partial T}{\partial t} = K_A \nabla^2 T + \rho_b C_b w_b (T-T_b) + P \quad r \{adrenal\ tissue\}z$$

$$P_F C_F \frac{\partial T}{\partial t} = K_A \nabla^2 T + \rho_b C_b w_b (T-T_b) + P \quad r \{fat\ tissue\}$$

Figure S3 is demonstrating the model geometry and main results.

Table S1. Physical parameters used in the FEM modeling

Parameter	Value
Blood density, ρ_b	1000 kg/m^3
Heat capacity blood, $C_{p,b}$	4180 J/(kg·K)
Blood perfusion rate, ω_b	0.0064 s^{-1}
Arterial blood temperature, T_b	37 °C
Initial and boundary temperature, T_0	37 °C
Heat capacity adrenal, $C_{p,A}$	3540 J/(kg·K)
Adrenal density, ρ_A	1020 kg/m^3
Adrenal thermal conductivity, k_A	0.52 W/(m·K)
Heat capacity fat, $C_{p,F}$	2348 J/(kg·K)
Fat density, ρ_F	911 kg/m^3
Fat thermal conductivity, k_F	0.21 W/(m·K)

SI-2: Standardization of adrenal gland images for the identification of injection locations

To identify the location of NPs injection in the adrenal gland following the surgical procedure, we analyzed 12 adrenal glands post-surgery, each with 1–3 MNP injections. Adrenal glands were sliced (Materials and Methods) and mounted on glass slides. All slices were imaged using a confocal microscope (Olympus), generating a mosaic scan of the entire gland using the Fluoview FV100 software (Olympus). The slices from the different injected glands varied in their structure due to the orientation of the gland during slicing, variation in different rats' gland structures and the gland extraction process post-perfusion. Therefore, an image analysis method was needed to automatically standardize the slices to be able to define the main substructures in each slice - medulla, zona glomerulosa (ZG), zona fasciculata (ZC) and zona reticularis (ZR).

A script was developed in Mathematica software (Wolfram Research) to create a geometric transformation procedure to map the varying adrenal gland slices to ellipses with the same semi-axes. The method differs from common image processing techniques in that it keeps the pixel values unchanged but rather modifies the pixels' positions. This procedure is general and can be further used as a map between any two simply connected shapes, i.e. without any holes, in which rays from the centroid intersect the boundary once (the simplest case being two convex shapes). The adrenal gland was first rotated such that its largest axis is oriented along the horizontal axis and binarized to create a convex mask. A non-uniform rational B-spline (NURBS) interpolation of the perimeter distance from the centroid (**Fig. S6**) was then performed from the binary mask. The geometric transformation was defined using the mapping:

$$f:(r,\theta) \mapsto \left(R(\vartheta)\frac{r}{perimeter(\vartheta)},\theta\right)$$

Where, the polar coordinates are referenced with regards to the image centroid, perimeter(ϑ) is the NURBS interpolation function evaluated at angle ϑ, and R(ϑ) is the ellipse perimeter. The mapping ensures that the relative positions of the image features are preserved, even if their sizes are allowed to vary. Once all slices were standardized to the same ellipse size, four masks were defined with dimensions of each substructure. For each slice, the 4 masks were applied counting if there was injection in that substructure and calculating the area of injection in each substructure (**Fig. S6**).

SI-3: Averaging the change in rat heart rate following the magnetothermal stimulation

The rat heart rate (in beats per minute, bpm) was recorded before, during and after magnetothermal stimulation using a Physiosuite system (Kent Scientific) with an optical sensor affixed to the hindlimb. Rats were anesthetized using isoflurane and transferred to the AMF coil. Due to the anesthesia, large fluctuations in heart rate were observed following the start of the anesthesia. Therefore, we allowed for at least 10 minutes for heart rate to stabilize prior to applying the AMF stimulus. Moreover, due to the anesthesia a monotonic decrease in heart rate baseline (*42*) was observed throughout the entire experiment duration in the absence of stimuli. Rats were stimulated for 40 s and the heart rate was recorded for at least 3 min after the end of the stimulation epoch.

In order to isolate the effects of the magnetothermal stimulation on the heart rate from the

decreasing baseline we performed time series filtering. A moving average of 50 s was applied to smooth the raw data, followed by a baseline estimation using a statistics-sensitive nonlinear iterative peak clipping (SNIP) algorithm as shown by the red line in **Figures S11A,D**. The baseline was subsequently subtracted from the filtered trace to highlight the deviations from the baseline (**Fig. S11B,E**). For scale comparison, the same area is shaded in **Figures S11A,D**. As demonstrated in the examples in **Figure S11**, an increase in heart rate was observed in the case of MNP-injected rats and was not observed in the case of WNP-injected rats. To quantify the rapid changes in the rat's heart rate during the AMF stimulation, we further performed a forward first-order finite difference to quantify the change in heart rate slope (**Fig. S11C,F**). In the case of rats injected with MNPs, a positive change in slope could be observed during and immediately after the AMF stimulation that was not identified in rats injected with WNPs (Main manuscript, **Fig. 6F-I**).

SI-4: Calculation of the mechanical effect from MNPs exposed to AMF

MNPs in an alternating magnetic field (AMF) are subject to a torque that can cause their physical rotation, which is termed Brownian relaxation, as opposed to a competing mechanism of magnetization reversal, Néel relaxation, in which the magnetic moment rotates independent of the MNP orientation, overcoming the magnetic anisotropy barrier (*34*). Both mechanisms lead to heat dissipation, and previous studies including our earlier work aimed at optimizing the hysteretic performance of MNPs in high frequency AMFs have concluded that Néel relaxation is the dominant mechanism for effective heat dissipation (*24*). If we nonetheless calculate the mechanical forces that could be produced by a single MNP, we find them to be quite negligible (*43*) in comparison to the force thresholds of mechanosensitive ion channels:

Brownian relaxation:

To know whether Brownian relaxation of the MNPs under AMFs might lead to forces induced on cells, we can compare the Brownian relaxation frequency(*44*) to the AMF frequency:

$$f_{Brown} = \frac{k_B T}{8\pi^2 \eta r_H^3} = \frac{\left(1.38 \times 10^{-23} \frac{J}{K}\right) 310K}{8\pi^2 (10^{-3} Pa\, s)(25 \times 10^{-9} m)^3} = 3.5 \times 10^3 \text{ Hz}$$

Where η is the dynamic viscosity of the extracellular environment and r_H is the hydrodynamic radius. This frequency is 0.7% of the AMF frequency (515 kHz). If a 22-nm diameter MNP were to rotate by 0.7% of 360 degrees, the linear rotation distance would be 0.7% of the

circumference, or 4.7 Å. We can also compute the energy that would be dissipated per cycle by this motion:

Moment of an individual MNP:

The average volume of a MNP used in this study is

$$V \approx \frac{4}{3}\pi r^3 = \frac{4}{3}\pi \times (11 \times 10^{-9}\ m)^3 = 5.6 \times 10^{-24}\ m^3.$$

The moment of a uniformly magnetized magnetite particle with that volume is:

$$|\vec{\mu}| = V \cdot \rho \cdot M_s = 5.6 \times 10^{-24}\ m^3 \left(\frac{5150\ kg}{m^3}\right)\left(\frac{83\ Am^2}{kg}\right) = 2.4 \times 10^{-18}\ Am^2$$

Where $\rho = 5150$ kg/m^3 and $M_s = 83$ Am^2/kg are the density and saturation magnetization of magnetite.

Torque:

The torque on a magnetic dipole in a uniform magnetic field is given by(*45*):

$$\vec{\tau} = \vec{\mu} \times \vec{B},$$

where $\vec{\mu}$ is the dipole moment and $\vec{B}$ is magnetic field.

Then the torque magnitude is:

$$|\vec{\tau}| = |\vec{\mu}||\vec{B}| \sin \theta_{\vec{\mu}-\vec{B}}$$

The maximum torque occurs when the angle between the magnetic moment and the applied field $(\theta_{\vec{\mu}-\vec{B}})$ is 90 degrees, in which case:

$$|\vec{\tau}| = |\vec{\mu}||\vec{B}|$$

For magnetic field of 19 mT (15 kA/m applied in our experiments) and a uniformly magnetized MNP:

$$|\vec{\tau}| = 2.4 \times 10^{-18}\ Am^2 \times 0.019\ T = 4.6 \times 10^{-20} Nm$$

Work done by torque:

$$W \approx \tau \Delta\theta = (4.6 \times 10^{-20} Nm\ )(0.042\ rad) = 1.9 \times 10^{-21} J$$

Which is about 0.5 $k_B T$. This is much smaller than the ~40 $k_B T$ necessary to activate the mechanosensitive ion channel such as Piezo1(*46*).

We could also consider aggregates of MNPs, which would have larger net moments and shape anisotropy that could lead to significant net torques. However, because the MNPs coated with PEG and form a stable ferrofluid they do not form permanent aggregates.
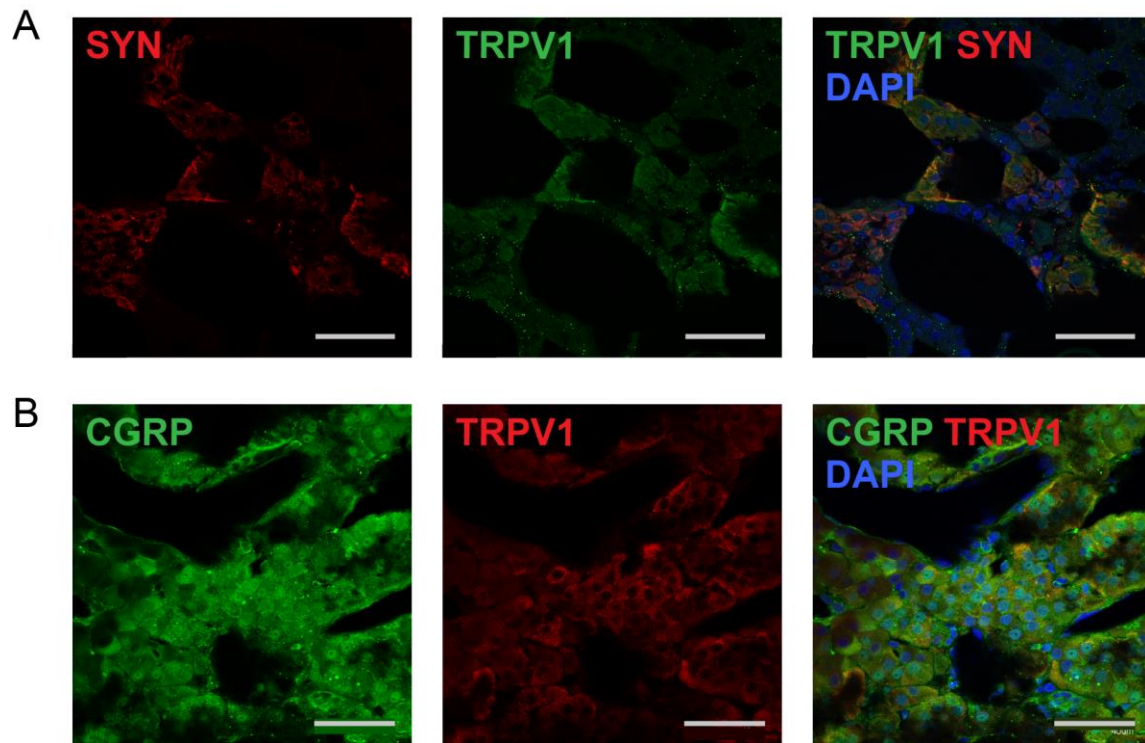
Figure S1 | Immunostaining of SYN and CGRP co-localization with TRPV1 in adrenal gland medulla. A, SYN (red), TRPV1 (green). **B,** CGRP (green), TRPV1 (red). Scale bar = 40 μm. Blue: DAPI.
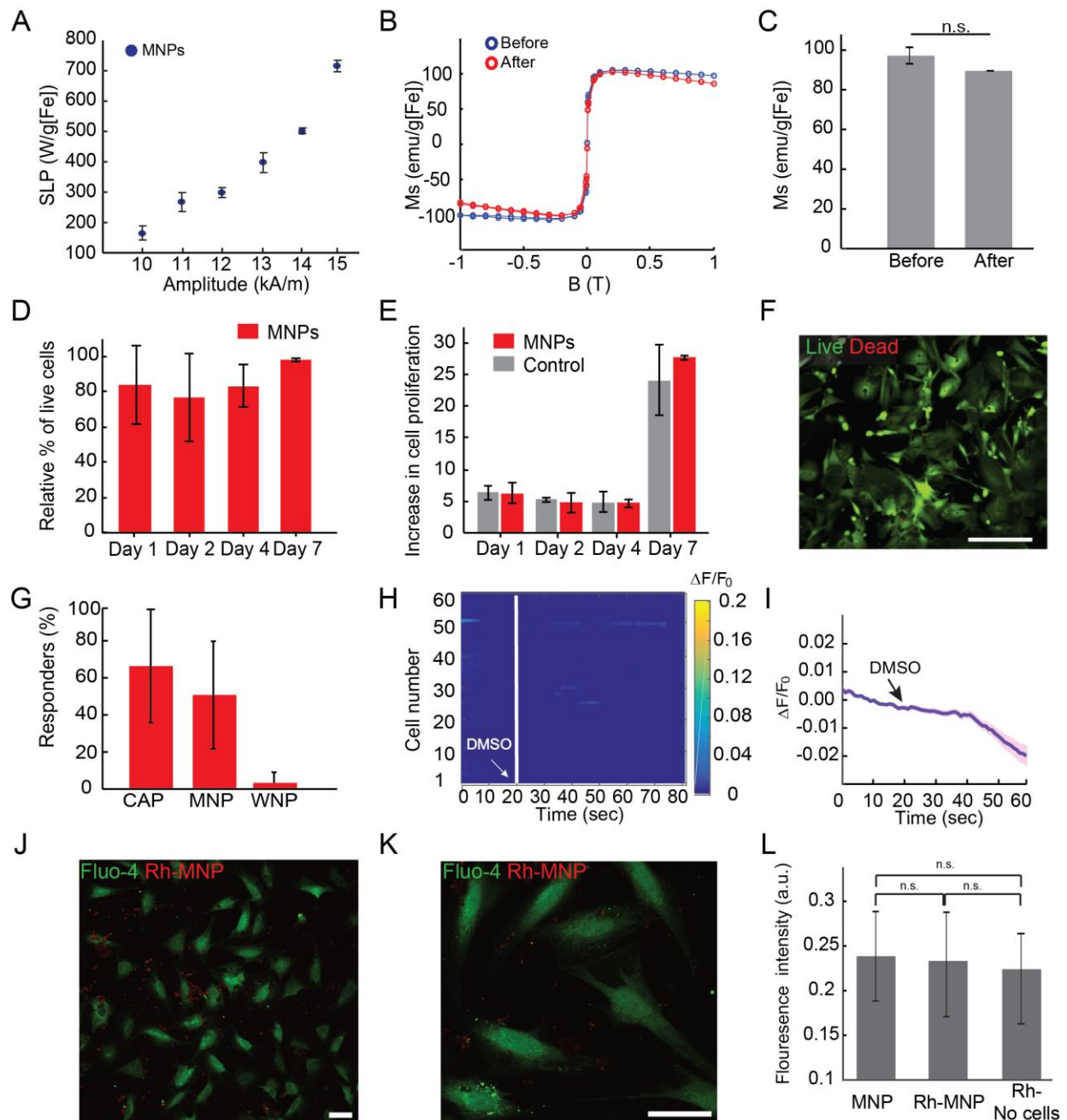
Figure S2 | Characterization of MNP properties and the response of a mixed adrenal culture to magnetothermal stimulation. A, Specific loss power (SLP) measured for MNPs at a frequency of 515 kHz and a range of amplitudes. **B,** Example of magnetization curves for MNPs before (blue) and after (red) 8 days of incubation in physiological conditions. **C,** calculated magnetization saturation of MNPs before and after incubation for 8 days in physiological conditions. Mean ± standard deviation. No significant difference was observed between the two groups (two-sided Student t-test, n=2). **D,** Biocompatibility alamarBlue assay. Percentage of live

cells compared to day 0 baseline values. MNPs were mixed in the cell medium and cells were incubated for 7 days. The alamarBlue test was repeated on days 1, 2, 4 and 7. All were compared to the day 0 baseline (n=4). **E,** Proliferation rate of adrenal cell cultures over 7 days compared to cells that were incubated with and w/o MNPs (n=4). **F,** Live/dead assay of adrenal cells after one day in culture. Green – live cells, red – dead cells. Different morphologies of cells can be recognized in the mixed adrenal culture. **G,** Percentage of responding cells in each examined condition out of total cells examined (n=5–9coverslips). Error bars are mean ± standard deviation **H,** Normalized Fluo-4 fluorescent intensity for 140 examined cells versus time in response to DMSO addition to the cell media. **I,** Average fluorescence change ΔF normalized to the average fluorescence F_0 during first 20 s ($\Delta F/F_0$) of cells responding to DMSO. Solid line = mean, shaded area = standard error of the mean (s.e.m.). **J,K,L,** Nanoparticle internalization into adrenal cells: MNPs labeled with Rhodamine (Rh) were incubated for 24 hours with adrenal cells. G,H, confocal images of adrenal cells labeled with Fluo-4 (green) and MNPs labeled with Rh (Rh-MNP, red). **K,** higher magnification confocal image of cells and MNPs. Only 11.6 ±3.1% (mean ± standard deviation) of total examined cells demonstrated labeled MNP internalization, suggesting that PEGylation resulted in minimal cell internalization in the conditions used in those experiments. **L,** Plate reader measurement of cells incubated with Rhodamine labeled MNPs, demonstrating non-significant change between the three examined groups: MNPs incubated with cells, Rh labeled MNPs incubi ted with cells and Rh-labeled MNPs incubated on Matrigel coverslips without cells.
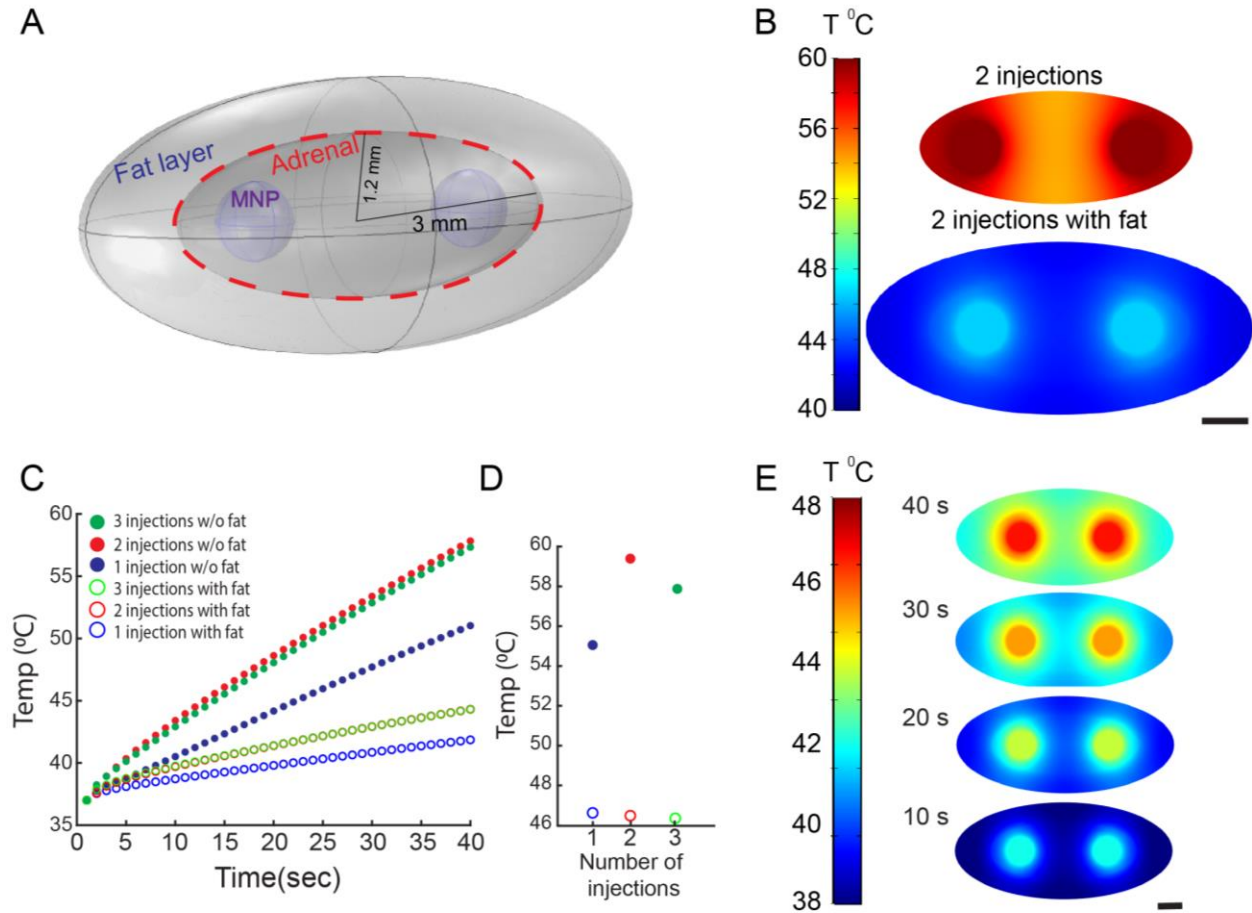
Figure S3 | Finite element model of heat distribution within adrenal gland during magnetothermal stimulation. A, Model geometry and dimensions with two MNP injection locations and adrenal gland surrounded by fat layer. **B,** Heat distribution map after 40 s of AMF stimulation inside adrenal gland injected with 0.8 µl MNPs (40 mg/ml) in two locations. Comparison of thermal distribution in adrenal glands without and with the surrounding 1.5 mm thick fat layer. Scale bar = 1 mm **C,** Temperature profile during 40 s AMF stimulation for adrenal glands injected with 1 µl /0.8 µl / 0.5 µl of MNPs in 1–3 locations respectively, w/ and w/o fat layer. **D,** Maximum temperature achieved in the gland after 40 s of AMF for 1–3 injections w/ and w/o fat layer. Comparison between 1, 2, and 3 injection sites. **E,** Heat distribution during 40 s AMF stimulation in adrenal gland injected with MNPs (40 mg/ml) in 2 locations. Scale bar = 1 mm
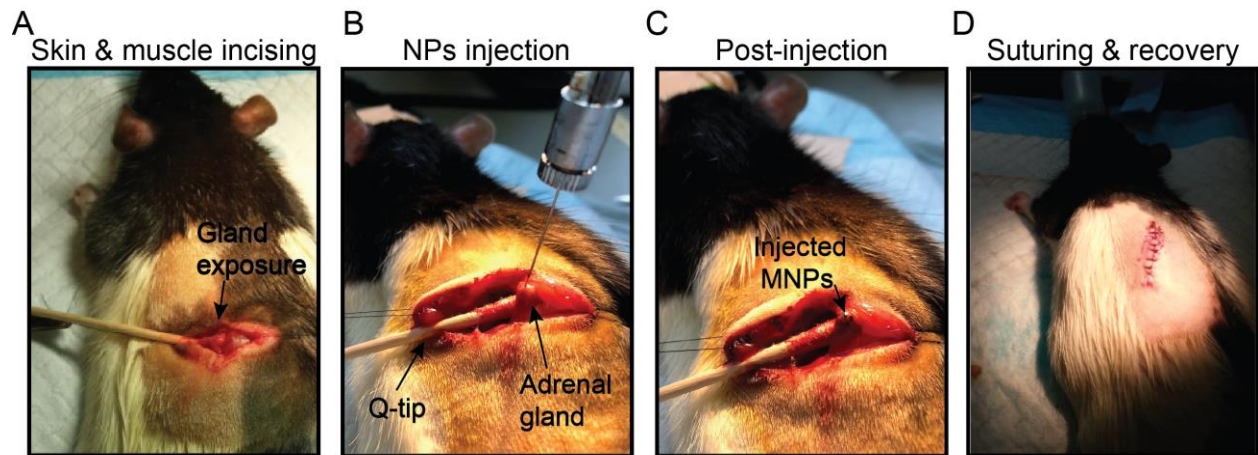
Figure S4 | Summary of surgical procedure for injecting MNPs directly into the rat's left adrenal gland. A, Skin and muscle incising on the rat's back. Adrenal gland is identified and exposed. **B,** After stabilization of the adrenal gland using a sterile Q-tip, an injection of 1 μl MNPs is performed via a microsyringe held in a stereotactic manipulator and inserted into the gland tissue. **C,** An image of adrenal gland immediately following injection, demonstrating two injection sites. **D,** Following the injection, muscle and skin are sutured and rats are allowed to recover for at least one week before AMF stimulation. (Photo Credit: Dekel Rosenfeld, Massachusetts Institute of Technology).
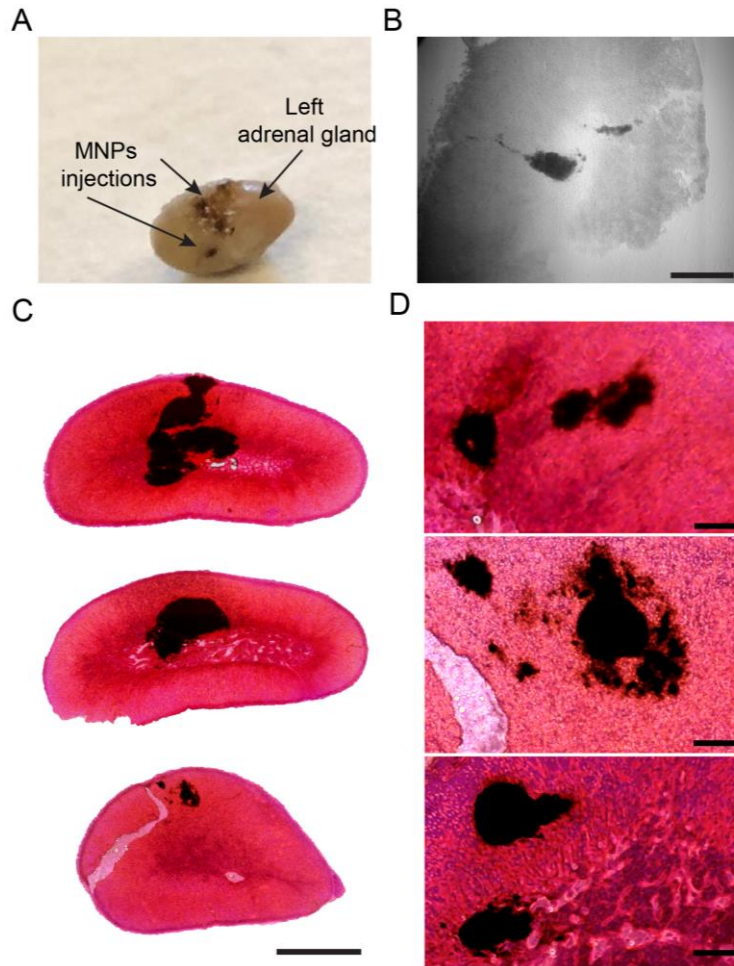
Figure S5 | Adrenal gland injected with MNPs and extracted from the rat 1-6 months following surgery. A, Micrograph of the entire adrenal gland immediately after extraction form the rat, 6 months post-injection, showing the locations of injections. No significant damage in the adrenal tissue was observed. **B,** Bright field image (10× magnification) of adrenal slice with MNPs 6 months post-injection. Adrenal gland was placed in 4% PFA overnight and sliced at 40 μm thickness. The MNPs could be observed inside the tissue even at 6 months after the injection surgery. Scale bar = 200 μm. **C,** H&E examples of adrenal slices of adrenal glands injected with MNPs and sliced 1-2 months post-injection. 1-3 injections sites with different sizes are observed. Minimal damage was observed in the tissue and the area surrounding the injection site. No immune response was observed from the presence of the biochemically inert iron oxide nanoparticles. Scale bar = 1 mm **D,** Higher magnification of adrenal gland slices stained for H&E demonstrating the injection sites of MNPs and the surrounding tissue. Scale bar= 200 μm. (Photo Credit: Dekel Rosenfeld, Massachusetts Institute of Technology).
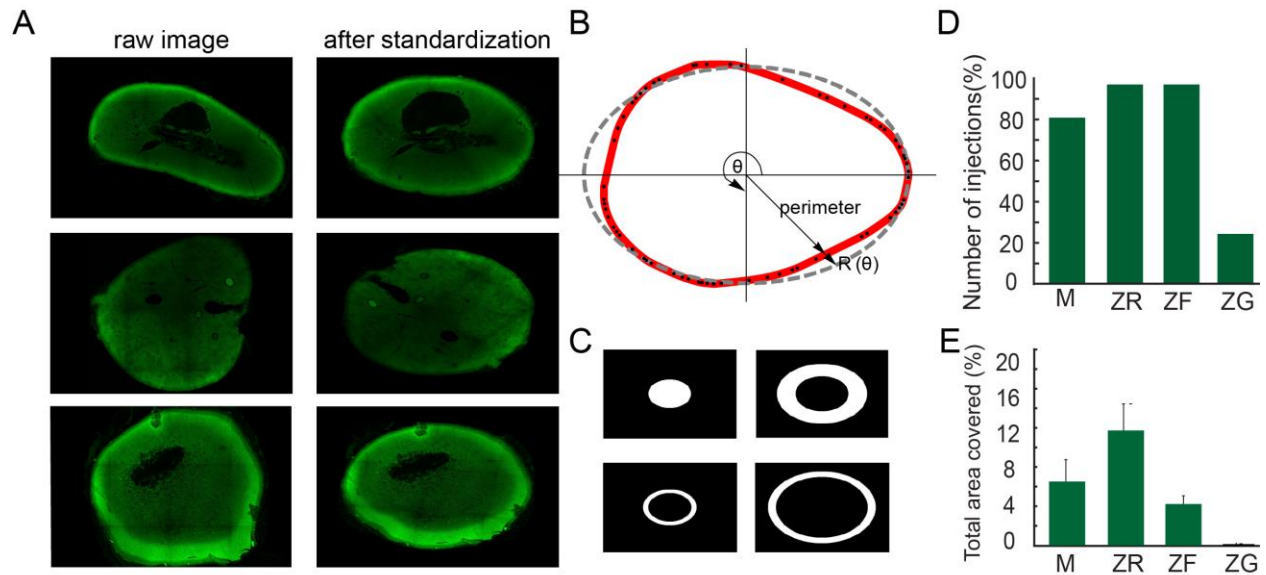
Figure S6 | Standardization process of adrenal gland slices for conversion to an ellipse with certain dimension for injection location examination. A, Examples of adrenal gland slices (out of n=12 examined slices) and their mapping onto generalized ellipse (SI-2). Left column- raw images. Right column – result of mapping. **B,** The principal of the statistics-sensitive nonlinear iterative peak clipping (SNIP) algorithm. **C,** Four masks were used to define the 4 substructures of the adrenal gland for consistent definition of the injection location within the gland. **D,** Percent of injection sites out of total examined location sites over 12 examined adrenal gland slices with 1–3 injection sites in each. **E,** total area covered by the MNPs in each substructure as quantified in 12 examined adrenal glands.
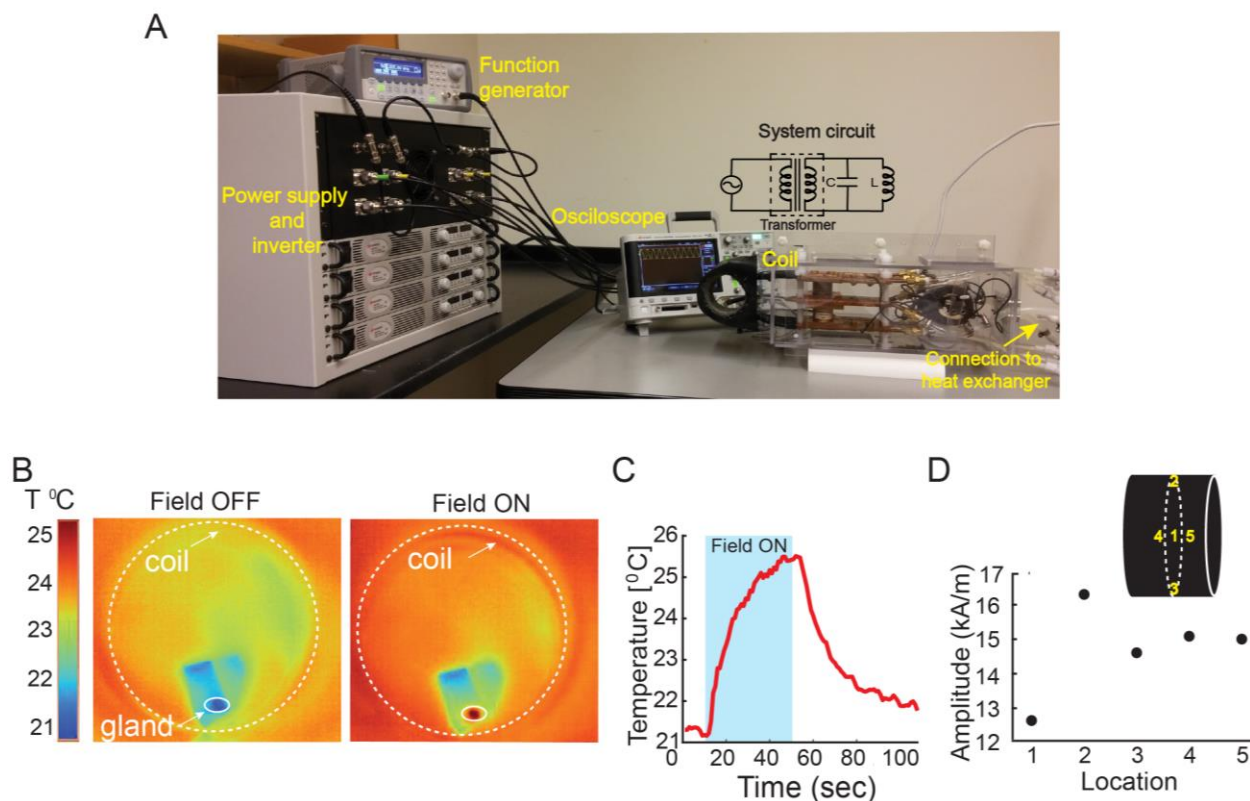
Figure S7 | Magnetothermal stimulation setup and system characterization. A, Components of the in vivo AMF stimulation setup. The circuit for the AMF coil is presented. The rat is placed within the coil during experiments. **B,** Temperature increase under AMF stimulation in extracted adrenal gland injected with three locations of MNPs (40 mg/ml), as measured with an infrared camera during the stimulation. The adrenal gland is located at the anticipated position of the rat adrenal gland in vivo. The experiment was conducted at room temperature and the temperature measured was largely from the adrenal gland surface. **C,** Temperature profile of the adrenal gland surface during the magnetothermal stimulation described in **B**. **D,** Measurement of AMF amplitude over 5 locations inside the coil driven with parameters similar to those described in the materials and methods. Locations on the middle axis of the coil are presented and the AMF amplitude was measured using a custom-designed pickup coil with a known geometry. (Photo Credit: Dekel Rosenfeld, Massachusetts Institute of Technology).
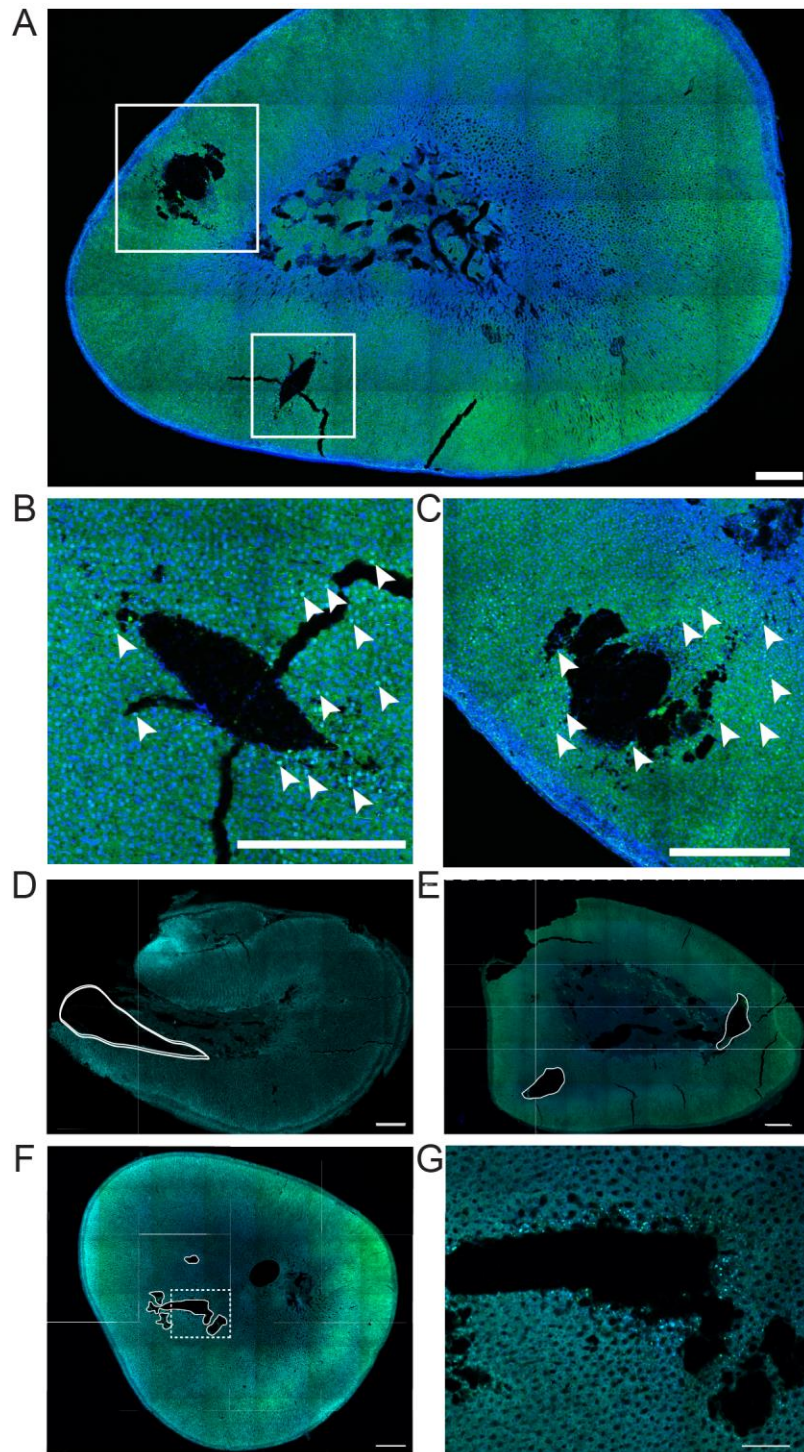
Figure S8 | c-Fos immunostaining following magnetothermal stimulation. A, A mosaic of an entire slice of an adrenal gland injected with MNPs in two locations (white squares). Green represents c-Fos; blue represents DAPI. **B, C,** A close-up view of the tissue encompassed by one

of the white squares in **A** demonstrates an increased *c-fos* expression (white arrows) in the area surrounding the MNPs injections. Scale bar = 300 μm. Mosaic scan was acquired with 20X oil immersion objective (NA=0.85) and processed using the FV1000 software (Olympus). **D-G,** Chronic implantation and stimulation of adrenal gland following MNPs injection. (**D-F**) A mosaic of an entire slice of an adrenal gland injected with MNPs after repeated stimulations (3-5 stimulations) over a period of up to two months. On the last stimulation, rat was perfused and adrenal gland were immunostained for the expression of c-Fos. Green represents c-Fos; blue represents DAPI. Scale bar 200 μm. No significant damage in the adrenal tissue was observed even after repeated magnetothermal stimulations. **G,** A close-up view of the tissue encompassed by the white square in **c** demonstrates an increased *c-fos* expression in the area surrounding the MNPs injections. Scale bar 50 μm.
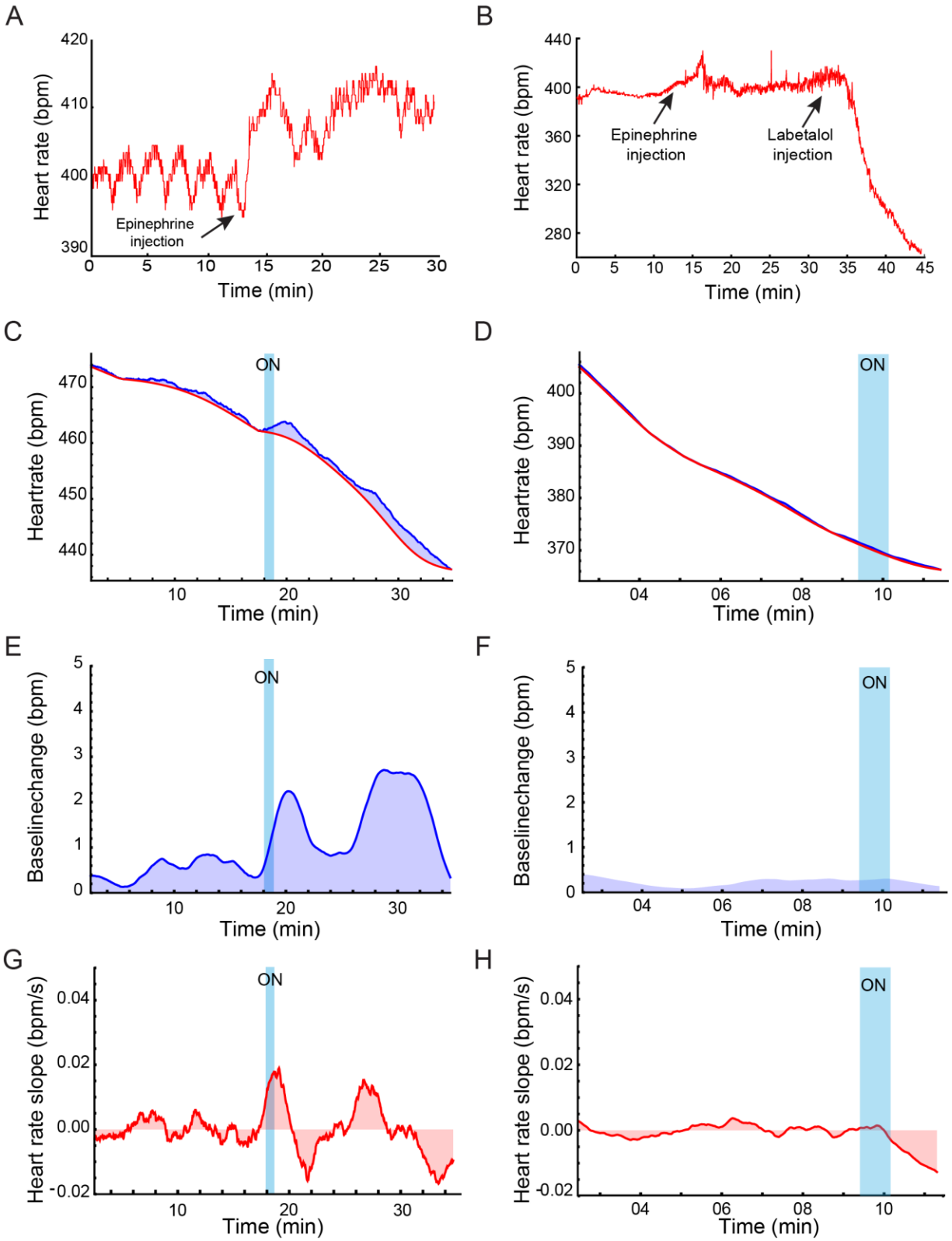
Figure S9 | Heart rate measurement A, B, Heart rate measurements in a naive rat. Response to systemic drug injection. Rats were injected with (**A**) Epinephrine alone or (**B**) epinephrine

followed by the beta-blocker labetalol. Heart rate was continuously measured using a Physiosuite equipped with an optical sensor affixed to the rat hindlimb. Heart rate increase could be observed immediately following epinephrine injection and a decrease was observed in response to the labetalol injection. **C-H,** Heart rate measurement and analysis following magnetothermal stimulation. A rat injected with MNPs (**A,E,G**) compared to a rat injected with WNPs (**D,F,H**). **C, D,** Heart rate values before, during and after AMF stimulation (marked ON). The blue curve represents the actual values and red curve represents the baseline estimation curve (**SI-3**). **E, F,** The change from baseline curve after baseline subtraction. **G, H,** Calculation of the heart rate slope before, during and after AMF stimulation, demonstrating a positive increase in the slope in the case of MNPs (**G**) not observed in the case of WNPs (**H**).

REFERENCES AND NOTES

1. M. G. Arnett, L. M. Muglia, G. Laryea, L. J. Muglia, Genetic approaches to hypothalamic-pituitary-adrenal axis regulation. *Neuropsychopharmacology* **41**, 245–260 (2015).

2. S. A. Kinlein, C. D. Wilson, I. N. Karatsoreos, Dysregulated hypothalamic–pituitary–adrenal axis function contributes to altered endocrine and neurobehavioral responses to acute stress. *Front. Psychol.* **6**, 31 (2015).

3. B. Hruska, P. K. Cullen, D. L. Delahanty, Pharmacological modulation of acute trauma memories to prevent PTSD: Considerations from a developmental perspective. *Neurobiol. Learn. Mem.* **112**, 122–129 (2014).

4. V. A. Pavlov, K. J. Tracey, The vagus nerve and the inflammatory reflex—Linking immunity and metabolism. *Nat. Rev. Endocrinol.* **8**, 743–754 (2012).

5. V. Pikov, A. Sridhar, H. E. Lara, High-frequency electrical modulation of the superior ovarian nerve as a treatment of polycystic ovary syndrome in the rat. *Front. Physiol.* **9**, 459 (2018).

6. V. Walsh, A. Cowey, Transcranial magnetic stimulation and cognitive neuroscience. *Nat. Rev. Neurosci.* **1**, 73–79 (2000).

7. J. O. Szablowski, A. Lee-Gosselin, B. Lue, D. Malounda, M. G. Shapiro, Acoustically targeted chemogenetics for the non-invasive control of neural circuits. *Nat. Biomed. Eng.* **2**, 475–484 (2018).

8. O. Yizhar, L. E. Fenno, T. J. Davidson, M. Mogri, K. Deisseroth, Optogenetics in neural systems. *Neuron* **71**, 9–34 (2011).

9. Q. A. Pankhurst, J. Connolly, S. K. Jones, J. Dobson, Applications of magnetic nanoparticles in biomedicine. *J. Phys. D. Appl. Phys.* **36**, R167 (2003).

10. H. Huang, S. Delikanli, H. Zeng, D. M. Ferkey, A. Pralle, Remote control of ion channels and neurons through magnetic-field heating of nanoparticles. *Nat. Nanotechnol.* **5**, 602–606 (2010).

11. R. Chen, G. Romero, M. G. Christiansen, A. Mohr, P. Anikeeva, Wireless magnetothermal deep brain stimulation. *Science* **347**, 1477–1480 (2015).

12. S. A. Stanley, J. E. Gagner, S. Damanpour, M. Yoshida, J. S. Dordick, J. M. Friedman, Radio-wave heating of iron oxide nanoparticles can regulate plasma glucose in mice. *Science* **336**, 604–608 (2012).

13. S. Schuerle, J. S. Dudani, M. G. Christiansen, P. Anikeeva, S. N. Bhatia, Magnetically actuated protease sensors for in vivo tumor profiling. *Nano Lett.* **16**, 6303–6310 (2016).

14. R. Munshi, S. M. Qadri, Q. Zhang, I. C. Rubio, P. del Pino, A. Pralle, Magnetothermal genetic deep brain stimulation of motor behaviors in awake, freely moving mice. *eLife* **6**, e27069 (2017).

15. Q. Yu, Y. Wang, Y. Yu, Y. Li, S. Zhao, Y. Chen, A. B. Waqar, J. Fan, E. Liu, Expression of TRPV1 in rabbits and consuming hot pepper affects its body weight. *Mol. Biol. Rep.* **39**, 7583–7589 (2012).

16. A. M. de Diego, L. Gandia, A. G. García, A physiological view of the central and peripheral mechanisms that regulate the release of catecholamines at the adrenal medulla. *Acta Physiol.* **192**, 287–301 (2008).

17. T. J. Rosol, J. T. Yarrington, J. Latendresse, C. C. Capen, Adrenal gland: structure, function, and mechanisms of toxicity. *Toxicol. Pathol.* **29**, 41–48 (2001).

18. A. G. García, A. M. García-De-Diego, L. Gandía, R. Borges, J. García-Sancho, Calcium signaling and exocytosis in adrenal chromaffin cells. **86**, 1093–1131 (2006).

19. J. J. Enyeart, J. A. Enyeart, Ca^{2+} and K^+ channels of normal human adrenal zona fasciculata cells: Properties and modulation by ACTH and AngII. *J. Gen. Physiol.* **142**, 137–155 (2013).

20. P. N. Surkin, S. L. Gallino, V. Luce, F. Correa, J. Fernandez-Solari, A. De Laurentiis, Pharmacological augmentation of endocannabinoid signaling reduces the neuroendocrine response to stress. *Psychoneuroendocrinology* **87**, 131–140 (2018).

21. B. Wiedenmann, W. W. Franke, Identification and localization of synaptophysin, an integral membrane glycoprotein of Mr 38,000 characteristic of presynaptic vesicles. *Cell* **41**, 1017–1028 (1985).

22. H. Kuramoto, H. Kondo, T. J. C. Fujita, Calcitonin gene-related peptide (CGRP)-like immunoreactivity in scattered chromaffin cells and nerve fibers in the adrenal gland of rats. *Cell Tissue Res.* **247**, 309–315 (1987).

23. R. Chen, M. G. Christiansen, A. Sourakov, A. Mohr, Y. Matsumoto, S. Okada, A. Jasanoff, P. Anikeeva, High-performance ferrite nanoparticles through nonaqueous redox phase tuning. *Nano Lett.* **16**, 1345–1351 (2016).

24. R. Chen, M. G. Christiansen, P. Anikeeva, Maximizing hysteretic losses in magnetic ferrite nanoparticles via model-driven synthesis and materials optimization. *ACS Nano* **7**, 8990–9000 (2013).

25. C. A. McCammon, Magnetic properties of Fe_xO ($x > 0.95$): Variation of Néel temperature. *J. Magn. Magn. Mater.* **104-107**, 1937–1938 (1992).

26. K. B. Helle, M.-H. Metz-Boutigue, M. C. Cerra, M. C. Cerra, T. Angelone, Chromogranins: From discovery to current times. *Pflugers Arch.* **470**, 143–154 (2018).

27. S. Bevan, S. Hothi, G. Hughes, I. F. James, H. P. Rang, K. Shah, C. S. J. Walpole, J. C. Yeats, Capsazepine: A competitive antagonist of the sensory neurone excitant capsaicin. *Br. J. Pharmacol.* **107**, 544–552 (1992).

28. M. G. Christiansen, C. M. Howe, D. C. Bono, D. J. Perreault, P. Anikeeva, Practical methods for generating alternating magnetic fields for biomedical research. *Rev. Sci. Instrum.* **88**, 084301 (2017).

29. M. J. Caterina, M. A. Schumacher, M. Tominaga, T. A. Rosen, J. D. Levine, D. Julius, The capsaicin receptor: A heat-activated ion channel in the pain pathway. *Nature* **389**, 816–824 (1997).

30. M. Marcus, M. Karni, K. Baranes, I. Levy, N. Alon, S. Margel, O. Shefi, Iron oxide nanoparticles for neuronal cell applications: Uptake study and magnetic manipulations. *J. Nanobiotechnology* **14**, 37 (2016).

31. M. Pelto-Huikko, Å. Dagerlind, S. Ceccatelli, T. Hökfelt, The immediate-early genes c-*fos* and c-*jun* are differentially expressed in the rat adrenal gland after capsaicin treatment. *Neurosci. Lett.* **126**, 163–166 (1991).

32. T. C. Wessel, T. H. Joh, Parallel upregulation of catecholamine-synthesizing enzymes in rat brain and adrenal gland: Effects of reserpine and correlation with immediate early gene expression. *Mol. Brain Res.* **15**, 349–360 (1992).

33. R. M. Sapolsky, L. M. Romero, A. U. Munck, How do glucocorticoids influence stress responses? Integrating permissive, suppressive, stimulatory, and preparative actions. *Endocr. Rev.* **21**, 55–89 (2000).

34. M. G. Christiansen, A. W. Senko, R. Chen, G. Romero, P. Anikeeva, Magnetically multiplexed heating of single domain nanoparticles. *Appl. Phys. Lett.* **104**, 213103 (2014).

35. M. G. Shapiro, K. Homma, S. Villarreal, C.-P. Richter, F. Bezanilla, Infrared light excites cells by changing their electrical capacitance. *Nat. Commun.* **3**, 736 (2012).

36. K. Talavera, K. Yasumatsu, T. Voets, G. Droogmans, N. Shigemura, Y. Ninomiya, R. F. Margolskee, B. Nilius, Heat activation of TRPM5 underlies thermal sensitivity of sweet taste. *Nature* **438**, 1022–1025 (2005).

37. T. Voets, K. Talavera, G. Owsianik, B. Nilius, Sensing with TRP channels. *Nat. Chem. Biol.* **1**, 85–92 (2005).

38. A. Akbar, Y. Yiangou, P. Facer, J. R. Walters, P. Anand, S. Ghosh, Increased capsaicin receptor TRPV1-expressing sensory fibres in irritable bowel syndrome and their correlation with abdominal pain. *Gut* **57**, 923–929 (2008).

39. E. S. Schwartz, J. A. Christianson, X. Chen, J. H. La, B. M. Davis, K. M. Albers, G. F. Gebhart, Synergistic role of TRPV1 and TRPA1 in pancreatic pain and inflammation. *Gastroenterology* **140**, 1283–1291.e1-e2 (2011).

40. P. K. Randhawa, A. S. Jaggi, TRPV1 channels in cardiovascular system: A double edged sword? *Int. J. Cardiol.* **228**, 103–113 (2017).

41. V. Koko, J. Djordjeviæ, G. Cvijiæ, V. Davidoviæ, Effect of acute heat stress on rat adrenal glands: A morphological and stereological study. *J. Exp. Biol.* **207**, 4225–4230 (2004).

42. T. Ledowski, B. Bein, R. Hanss, A. Paris, W. Fudickar, J. Scholz, P. H. Tonner, Neuroendocrine stress response and heart rate variability: A comparison of total intravenous versus balanced anesthesia. *Anesth. Analg.* **101**, 1700–1705 (2005).

43. M. Meister, Physical limits to magnetogenetics. *eLife* **5**, e17210 (2016).

44. J. Landers, S. Salamon, H. Remmer, F. Ludwig, H. Wende, Simultaneous study of brownian and néel relaxation phenomena in ferrofluids by mössbauer spectroscopy. *Nano Lett.* **16**, 1150–1155 (2016).

45. D. J. Griffiths, in *Introduction to Electrodynamics,* D. J. Griffiths, Ed. (Cambridge Univ. Press, 2017), pp. 266–295.

46. C. D. Cox, C. Bae, L. Ziegler, S. Hartley, V. Nikolova-Krstevski, P. R. Rohde, C.-A. Ng, F. Sachs, P. A. Gottlieb, B. Martinac, Removal of the mechanoprotective influence of the cytoskeleton reveals PIEZO1 is gated by bilayer tension. *Nat. Commun.* **7**, 10366 (2016).